INORGANIC CHEMISTRY FRONTIERS

RESEARCH ARTICLE

View Article Online
View Journal | View Issue

Check for updates

Cite this: *Inorg. Chem. Front.*, 2024, **11**, 7475

# Variable energy transfer in one-dimensional chiral Mn/Cd-based halides and strong stereo-selective fluorescence for chiral recognition†

Sidan Wang, ‡[a] Pei Wang, ‡[a] Guojun Zhou, *[a] Nan Zhang,[a] Yilin Mao[a] and Xian-Ming Zhang *[a,b]

Low-dimensional chiral metal halides (CMHs) are promising as an industrialized platform for chiral recognition applications; however, there are hardly any luminescent CMHs with variable energy transfer between an organic ligand and an inorganic unit. Herein, an array of rare one-dimensional (1D) luminescent CMHs were engineered by screening *R*/*S*-3-aminopiperidine dihydrochloride as a chiral template, in which the chirality of the organic cation is transferred to the inorganic chain *via* hydrogen bonding interactions in (*R*/*S*-$C_5H_{14}N_2$)$MCl_4{\cdot}H_2O$ (M = Mn, Cd), abbreviated as *R*/*S*-Mn and *R*/*S*-Cd. The orange emission at 607 nm is attributed to the d–d transition $^4T_1(G)-{}^6A_1(S)$ of $Mn^{2+}$ in *R*/*S*-Mn, along with an energy transfer from the organic cation to the inorganic chain. In contrast, a reverse energy transfer from the inorganic chain to the organic cation was verified in *R*/*S*-Cd, with the emission at 401 nm being attributed to the singlet self-trapped excitons (STEs) of $Cd^{2+}$. Beyond that, we innovatively proposed that the fluorescence quenching behaviour contributes to the strong stereo-selective fluorescence responsivity for mandelic acid (MA), confirming that *R*/*S*-Mn and *R*/*S*-Cd are useful for the rapid recognition of *R*/*S*-MA. This research not only promotes the discovery of low-dimensional luminescent CMHs but also expands their applications in bio-detection and sensing.

Received 6th July 2024,
Accepted 11th September 2024

DOI: 10.1039/d4qi01703j

rsc.li/frontiers-inorganic

Published on 12 September 2024. Downloaded on 6/17/2026 6:25:38 PM.

## Introduction

Introducing chirality into metal halides promises to trigger superior properties, including circular dichroism (CD),[1,2] circularly polarized luminescence (CPL),[3–7] second-harmonic generation (SHG),[8–10] spin-dependent transport,[11,12] *etc.*, which opens a great avenue for bio-detection and sensing,[13–15] optoelectronic devices[16,17] and spintronics.[18] Recently, chiral metal halides (CMHs) have been found to be a promising industrialized platform for chiral recognition applications; however, there are few CMHs emitters with energy transfer between the organic ligand and the inorganic unit, and their electron-transition mechanisms remain unclear.[19]

Chirality transfer from organic cations to inorganic units can be implemented not only by chemical bonding but also by intermolecular interactions, which opens structural possibilities for the development of CMHs with intrinsic non-central symmetry.[20,21] CMHs consist of an organic cation at the A-site, a metal cation at the B-site, and a halogen anion at the X-site. The B-site metals in CMHs focusing on $Sn^{2+}$, $Sb^{3+}$, $Bi^{3+}$, *etc.* with $ns^2$ electronic configuration,[6,22–25] $Cu^+$ and $Cd^{2+}$ with $d^{10}$ electronic configuration,[26,27] and $Mn^{2+}$ with $d^5$ electronic configuration[28] play a crucial role in dominating the optical properties. In particular, $Mn^{2+}$-based CMHs have achieved periodical progress in the field of chiral luminescence, where the luminescent colors depend on the coordination environment of $Mn^{2+}$. The four-coordinated $Mn^{2+}$ exhibits narrow-band green-yellow emission and the six-coordinated $Mn^{2+}$ exhibits broad-band orange-red emission, which is attributed to the d–d transition ($^4T_1 \rightarrow {}^6A_1$) of $Mn^{2+}$.[29–32] The CMHs can be classified as zero-dimensional (0D) isolated, one-dimensional (1D) chain, two-dimensional (2D) layered and three-dimensional (3D) networked structures at the molecular level,[33–35] in which the 1D luminescent CMHs are extremely rare. It should be noted that the construction of 1D Mn-based CMHs by Mao *et al.*[36] has greatly contributed to the chemical diversity in CMHs, but they only focused on the CPL behaviour, whose application scenarios urgently need to be expanded. Besides,

[a]*Key Laboratory of Magnetic Molecules and Magnetic Information Materials (Ministry of Education), School of Chemistry and Material Science, Shanxi Normal University, Taiyuan 030031, China. E-mail: zhougj@sxnu.edu.cn, zhangxm@dns.sxnu.edu.cn*

[b]*College of Chemistry & Chemical Engineering, Key Laboratory of Interface Science and Engineering in Advanced Material, Ministry of Education, Taiyuan University of Technology, Taiyuan, Shanxi 030024, P. R. China*

†Electronic supplementary information (ESI) available: Details of methods and additional figures and tables. CCDC 2359935–2359938. For ESI and crystallographic data in CIF or other electronic format see DOI: https://doi.org/10.1039/d4qi01703j

‡These two authors as co-first authors contributed equally to this work.

Published on 12 September 2024. Downloaded on 6/17/2026 6:25:38 PM.

research on $Cd^{2+}$-based CMHs is extremely restricted due to the lack of emphasis on the potential self-trapped excitons (STEs) emission. In this context, the discovery of 1D luminescent CMHs is proving to be challenging, while exploring their internal energy transfer and developing their applications in the field of chiral recognition are imminent.

Herein, an array of 1D luminescent CMHs were engineered by using *R*/*S*-3-aminopiperidine dihydrochloride as a chiral template. Asymmetric hydrogen bonding interactions between organic/inorganic blocks lead to symmetry breaking and helical distortion, promoting chirality transfer from the organic cation to $(R/S\text{-}C_5H_{14}N_2)MCl_4{\cdot}H_2O$ (M = Mn, Cd), abbreviated as *R*/*S*-Mn and *R*/*S*-Cd. The excited $3d^5$ electrons of $Mn^{2+}$ contribute to the orange emission at 607 nm from the d–d transition of $^4T_1(G)$–$^6A_1(S)$ in *R*/*S*-Mn and an energy transfer from the organic cation to the inorganic chain. The emission at 401 nm is attributed to the singlet STEs under the strong electron–phonon coupling in *R*/*S*-Cd, along with a reverse energy transfer from the inorganic chain to the organic cation. Beyond that, the fluorescence quenching behaviour was emphasized due to the strong stereo-selective responsivity between CMHs and mandelic acid (MA), confirming that the above CMHs are useful for the rapid identification of *R*/*S*-MA. This work provides new insights into the chiral fluorescence in CMHs and expands its application in chiral recognition.

## Experimental section

### Materials and preparation

All chemicals including $R\text{-}C_5H_{14}N_2Cl_2$ (98%, Aladdin), $S\text{-}C_5H_{14}N_2Cl_2$ (98%, Aladdin), $MnCl_2$ (99%, Aladdin), $CdCl_2$ (99%, Aladdin), HCl (36.5%, A.R.), $C_2H_5OH$ (99%, A.R.), $CH_3CN$ (acetonitrile, 99%, A.R.), and *R*/*S*-MA (*R*/*S*-mandelic acid, 99%, Energy Chemicals) were used without any further purification.

$(R/S\text{-}C_5H_{14}N_2)MCl_4{\cdot}H_2O$ (M = Mn, Cd) were synthesized by a cooling crystallization method, whose chemical formulae are abbreviated as *R*/*S*-Mn and *R*/*S*-Cd. As for *R*/*S*-Mn, $MnCl_2$ (0.3 mmol) and $R/S\text{-}C_5H_{14}N_2Cl_2$ (0.3 mmol) were dissolved in a mixture of $C_2H_5OH$ (1 mL) and HCl (1 mL). The solution was then heated at 70 °C and dissolved with stirring until clarified. The pale-pink needle-like single crystals were precipitated after the solution was slowly cooled to room temperature (RT). As for *R*/*S*-Cd, $CdCl_2$ (0.3 mmol) and $R/S\text{-}C_5H_{14}N_2Cl_2$ (0.3 mmol) were dissolved in a mixture of $C_2H_5OH$ (0.5 mL) and HCl (0.5 mL). The solution was stirred at 70 °C until the solution was clarified. The single crystals were synthesized after cooling to RT.

### Characterization

Single-crystal X-ray diffraction (SXRD) data of *R*/*S*-Mn were collected by using an XtaLAB AFC12 diffractometer (Rigaku) with Cu-Kα radiation ($\lambda$ = 1.54184 Å). SXRD data of *R*/*S*-Cd were collected by using a D8 Venture diffractometer (Bruker) with Mo-Kα radiation ($\lambda$ = 0.71073 Å). Powder X-ray diffraction (PXRD) patterns of *R*/*S*-Mn and *R*/*S*-Cd were collected by using a MiniFlex600 diffractometer (Rigaku) with Cu-Kα radiation ($\lambda$ = 1.5406 Å), operating at 40 kV and 15 mA. Photoluminescence (PL) spectra, photoluminescence excitation (PLE) spectra, and PL decay curves were recorded using a FLS920 fluorescence spectrophotometer (Edinburgh Instruments Ltd, UK). Circular dichroism (CD) spectra were collected by using a J-1500 circular dichroism spectrometer (JASCO). The morphology observation and elemental mappings were recorded by using a scanning electron microscope (SEM, Pharos).

### Theoretical calculations

Density functional theory (DFT) calculations were performed by using the Vienna *Ab initio* simulation package (VASP) code.[37,38] The Heyd–Scuseria–Ernzerhof functional (HSE06) was used to calculate the electronic properties.[39] The projector-augmented wave function (PAW) method was used to describe the electron–ion interaction.[40] The convergence criterion was the energy difference between two consecutive steps of the calculations to be less than $10^{-6}$ eV. The cut-off energy for the planewave function was set to 400 eV. The atom coordinates were fully optimized until the residual forces were less than 0.01 eV $Å^{-1}$.

## Results and discussion

$(R/S\text{-}C_5H_{14}N_2)MCl_4{\cdot}H_2O$ (M = Mn, Cd) were synthesized by using $R/S\text{-}C_5H_{14}N_2Cl_2$ as the chiral template, abbreviated as *R*/*S*-Mn and *R*/*S*-Cd. The crystallographic data are listed in Tables S1 and S2,† which can be deposited at the Cambridge Crystallographic Data Centre (CCDC 2359935–2359938†). *R*/*S*-Mn belongs to the monoclinic $P2_1$ space group with a 1D chain structure (Fig. 1a), where each Mn atom is coordinated to five Cl atoms and one O atom in a water molecule. The bond lengths and bond angles of *R*/*S*-Mn are slightly distinct, as listed in Tables S3 and S4.† The six-coordinated octahedral $[MnCl_5O]$ is formed as a serrated 1D chain by sharing Cl atoms, separated by the organic cations of $[R/S\text{-}C_5H_{14}N_2]^{2+}$ *via* intermolecular interactions. The helical inorganic chains (Fig. 1b) indicate that the Mn1 and Cl2 in the strongly distorted octahedron are coordinated to form a right-handed helix $[–Mn1–Cl2–]_\infty$ along the *b*-axis in *R*-Mn, whereas a left-handed helix $[–Mn1–Cl2–]_\infty$ along the *b*-axis is developed in *S*-Mn. Fig. 1c shows the asymmetric hydrogen bonding interactions between the organic cation and the inorganic chain, where each protonated N atom of $[R/S\text{-}C_5H_{14}N_2]^{2+}$ forms the N–H···Cl hydrogen bonding interaction with Cl (Table S5†). The Hirshfeld surfaces[41,42] of organic cations shown in Fig. S1a and b† were employed to analyse the intermolecular interactions in *R*-Mn and *S*-Mn, where the red regions on the Hirshfeld surface indicate the intense intermolecular interactions of H···Cl. The 2D fingerprint plots of H···Cl in *R*-Mn and *S*-Mn (Fig. 1c) represent the contributions of H···Cl interactions as 48.1% and 48.2%, respectively, proving the hydrogen bonding interactions on the construction of 1D $Mn^{2+}$-based CMHs.

 This journal is © the Partner Organisations 2024

Published on 12 September 2024. Downloaded on 6/17/2026 6:25:38 PM.

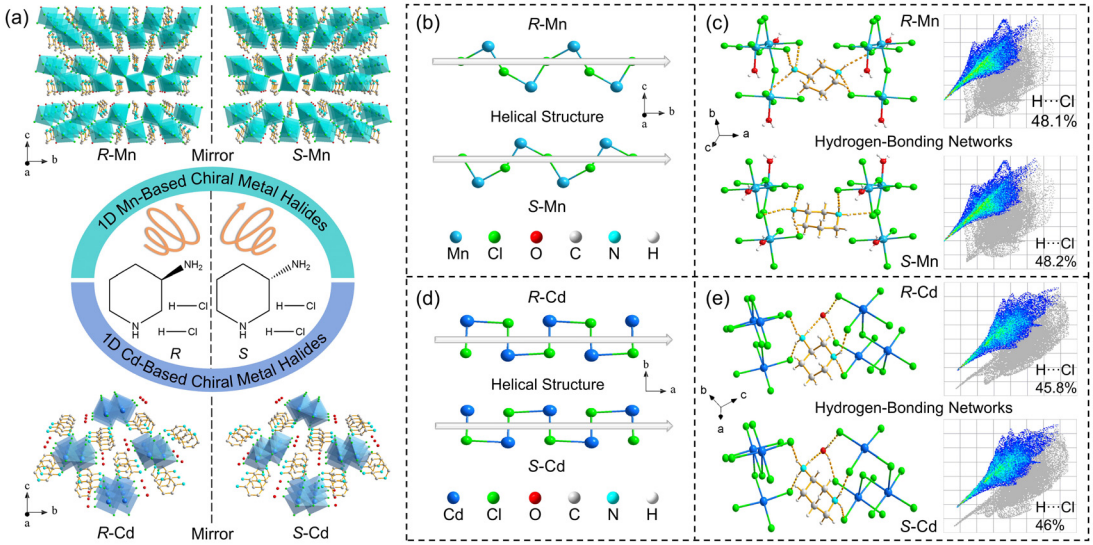


**Fig. 1** (a) Crystal structures of *R*/*S*-Mn and *R*/*S*-Cd. H atoms are omitted for clarity. (b) Right-handed helical structure in *R*-Mn and the left-handed helical structure in *S*-Mn. (c) Hydrogen bonding structures and 2D fingerprint plots of H···Cl in *R*/*S*-Mn. (d) Right-handed helical structure in *R*-Cd and the left-handed helical structure in *S*-Cd. (e) Hydrogen bonding structures and 2D fingerprint plots of H···Cl in *R*/*S*-Cd.

In contrast, *R*/*S*-Cd belongs to the orthorhombic $P2_12_12_1$ space group, in which each Cd atom is coordinated to five Cl atoms, which are connected by the shared Cl atom to form a 1D helical structure. The main bond lengths and bond angles are listed in Tables S6 and S7.† The helical inorganic units (Fig. 1d) indicate that Cd1 and Cl1 are coordinated to form a $[–Cd1–Cl1–]_\infty$ right-handed helical structure along the *a*-axis in *R*-Cd, whereas a $[–Cd1–Cl1–]_\infty$ left-handed helical structure is formed along the *a*-axis in *S*-Cd. The 1D chains in *R*/*S*-Cd are separated by the organic cation $[R/S\text{-}C_5H_{14}N_2]^{2+}$, whose organic and inorganic blocks are connected by N–H···Cl interactions, as shown in Fig. 1e and Table S8.† The Hirshfeld surface (Fig. S1c and d†) was further analysed based on the intermolecular interactions in *R*-Cd and *S*-Cd, and the 2D fingerprint plots of H···Cl (Fig. 1e) represent the contributions of H···Cl interactions as 45.8% and 46%. In addition, the organic cation interacts with the crystalline water *via* N–H···O hydrogen bonding, and the contribution of H···O interactions is 7.7%, which is conducive to fixing the organic cation to ensure the stability of the crystal framework. PXRD patterns and elemental mapping images (Fig. S2 and S3†) suggest the phase purity and the associated chemical compositions of *R*/*S*-Mn and *R*/*S*-Cd.

Considering that chiral materials possess distinct absorption capacities for left- and right-handed circularly polarized light, the solid-state CD spectra and UV-vis absorption spectra were recorded. The mirror-symmetric CD signals of *R*/*S*-Mn (Fig. 2a) appear in the corresponding absorption ranges, peaked at 244, 315 and 526 nm, respectively. In contrast, the mirror-symmetric CD signals of *R*/*S*-Cd (Fig. 2c) are observed at 236 nm and 320 nm. It is noted that pure *R*/*S*-3-aminopiperidine dihydrochloride only appears as CD peaks in the

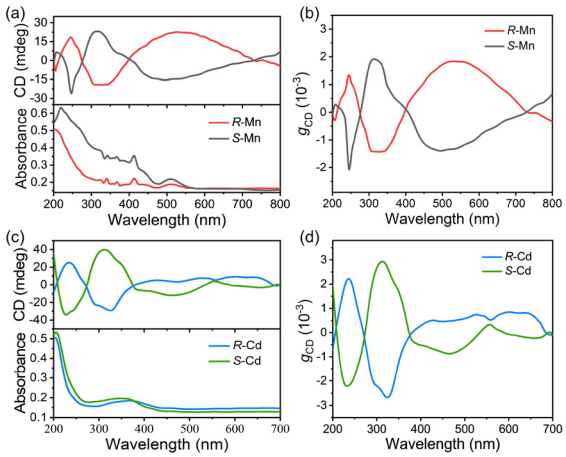


**Fig. 2** (a) The solid-state CD spectra and absorption spectra of *R*/*S*-Mn. (b) The $g_{CD}$ spectra of *R*/*S*-Mn. (c) The solid-state CD spectra and absorption spectra of *R*/*S*-Cd. (d) The $g_{CD}$ spectra of *R*/*S*-Cd.

200–300 nm range.[43] The CD difference between *R*/*S*-M (M = Mn, Cd) and $[R/S\text{-}C_5H_{14}N_2]^{2+}$ indicates that the chirality of the organic cation was transferred to the 1D chain building blocks. The CD intensity can be quantified by the absorption asymmetry factor $g_{CD}$:[44]

$$g_{CD} = \mathrm{CD[mdeg]}/(32\,980 \times \mathrm{absorbance}) \quad (1)$$

The maximum $|g_{CD}|$ of *R*-Mn and *S*-Mn were calculated to be $1.5 \times 10^{-3}$ and $2.0 \times 10^{-3}$ (Fig. 2b). The maximum $|g_{CD}|$ were calculated to be $2.3 \times 10^{-3}$ and $3.1 \times 10^{-3}$ for *R*-Cd and *S*-Cd (Fig. 2d). Fig. S4† shows the CPL spectra of *R*/S-Mn at RT.

Published on 12 September 2024. Downloaded on 6/17/2026 6:25:38 PM.

But there is no CPL signal for *R*/*S*-Cd. The emission dissymmetric extent is quantified by the dissymmetric factor ($g_{lum}$):

$$g_{lum} = 2(I_L - I_R)/(I_L + I_R) \quad (2)$$

where $I_L$ and $I_R$ represent the luminescence intensity of left and right circularly polarized light. The highest $g_{lum}$ of *R*-Mn and *S*-Mn are $7.52 \times 10^{-3}$ and $-5.19 \times 10^{-3}$, respectively.

As shown in Fig. 3a, the excitation peaks of *R*/*S*-Mn appear at 260, 268, 330, 350, 366, 416, 439, and 450 nm, corresponding to the electron transitions from the $Mn^{2+}$ ground state at $^6A_1(S)$ to the excited states at $^4A_2(F)$, $^4T_1(F)$, $^4T_1(P)$, $^4E(D)$, $^4T_2(D)$, [$^4A_1(G)$, $^4E(G)$], $^4T_2(G)$ and $^4T_1(G)$, respectively. They exhibit single-peak emission at 607 nm under low energy excitation, while they present double-peak emission at 433 nm and 607 nm under high energy excitation. The orange emission at 607 nm is attributed to the $^4T_1(G)$–$^6A_1(S)$ transition of six-coordinated $Mn^{2+}$. The blue emission at 433 nm is attributed to the singlet-state transition of the organic ligand (Fig. S5a†). Moreover, the energy transfer between the organic cation and the inorganic unit is verified due to the remarkable spectral overlap of PL peaked at 433 nm and PLE monitored at 607 nm (Fig. 3a), with the organic cation acting as a donor and the inorganic 1D chain as an acceptor. The energy transfer was further confirmed by the temperature-dependent PL spectra (Fig. S6†), especially for *R*/*S*-Mn. The PL decay curves of *R*/*S*-Mn can be fitted with a double exponential function (3), and the average lifetimes can be calculated using eqn (4):

$$I(t) = I_0 + A_1 \exp(-t/\tau_1) + A_2 \exp(-t/\tau_2) \quad (3)$$

$$\tau = (A_1\tau_1^2 + A_2\tau_2^2)/(A_1\tau_1 + A_2\tau_2) \quad (4)$$

where $I$(t) and $I_0$ are the PL intensity at time $t$ and $t \gg \tau$, respectively. $A$ is a constant and $t$ is the decay time of the exponential component. As shown in Fig. 3b, the lifetime of *R*/*S*-Mn monitored at 607 nm is 0.29 ms, indicating that it is attributed to the d–d transition of $Mn^{2+}$. The lifetime of *R*/*S*-Mn monitored at 433 nm is a uniform nanosecond level as the organic ligand (Fig. S5b†), thus demonstrating that the high-energy emission at 433 nm originates from the organic cation of $[R/S\text{-}C_5H_{14}N_2]^{2+}$. The excitation wavelength-dependent PL spectra of *R*/*S*-Mn (Fig. 3c) indicate that the high-energy emission at 433 nm disappears at the excitation wavelength from 410 nm to 450 nm. It is concluded that the PL emission peaks at 433 nm and 607 nm are attributed to the different electron-transition channels in *R*/*S*-Mn.

As shown in Fig. 3e, *R*/*S*-Cd exhibits a narrow emission peak at 401 nm under excitation at 287 nm, with a full width at half-maximum (FWHM) of 34 nm. The additional emission at 424 nm is presented under 350 nm excitation, along with a FWHM of 72 nm. The lifetime monitored at 424 nm is calculated to be 4.24 ns by fitting the PL decay curve (Fig. 3f) with the double exponential eqn (3) and (4), which is close to that of the organic ligand (Fig. S5b†), confirming its origin from the singlet-state transition ($S_1$–$S_0$) of $[R/S\text{-}C_5H_{14}N_2]^{2+}$. The lifetime monitored at 401 nm is calculated to be 433 ns by fitting the PL decay curve (Fig. 3f) with the single exponential eqn (5).

$$I(t) = I_0 + A\exp(-t/\tau) \quad (5)$$

We consider that the high-energy emission at 401 nm is attributed to the singlet STEs emission of $Cd^{2+}$. Based on that, the bond length distortion ($\Delta d$) of *R*/*S*-Cd is calculated by using eqn (6):

$$\Delta d = \frac{1}{5}\sum_{i=1}^{5}\left(\frac{d_n - d}{d}\right)^2 \quad (6)$$

where $d_n$ and $d$ represent the individual and average bond lengths of Cd–Cl. The $\Delta d$ of *R*-Cd and *S*-Cd are calculated to be

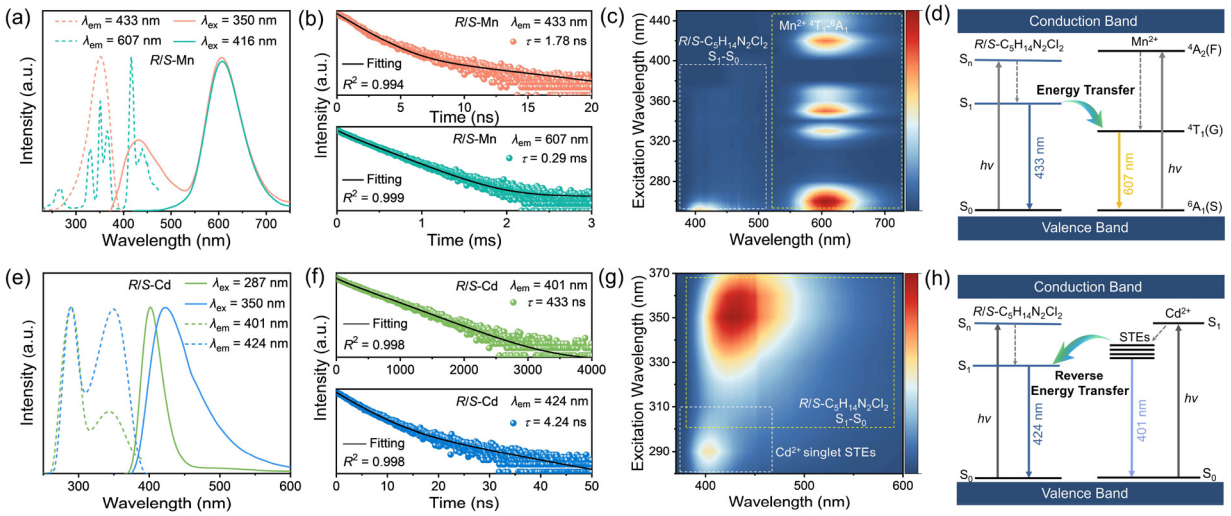


**Fig. 3** (a) PLE and PL spectra of *R*/*S*-Mn, and the remarkable spectral overlap of PL peaked at 433 nm and PLE monitored at 607 nm. (b) PL decay curves of *R*/*S*-Mn monitored at 433/607 nm emission. (c) Excitation wavelength-dependent PL spectra of *R*/*S*-Mn. (d) Schematic of the photo-physical mechanism in *R*/*S*-Mn. (e) PLE and PL spectra of *R*/*S*-Cd. (f) PL decay curves of *R*/*S*-Cd monitored at 401/424 nm emission. (g) Excitation wavelength-dependent PL spectra of *R*/*S*-Cd. (h) Schematic of the photo-physical mechanism in *R*/*S*-Cd.

 This journal is © the Partner Organisations 2024

Published on 12 September 2024. Downloaded on 6/17/2026 6:25:38 PM.

$2.93 \times 10^{-3}$ and $2.86 \times 10^{-3}$, respectively. The stronger distortion contributes to the formation of STEs. The temperature-dependent PL spectra of *R*/*S*-Cd under 287 nm excitation are shown in Fig. S7a,† and the degree of electron–phonon coupling is evaluated based on the Huang–Rhys factor ($S$) using eqn (7):[45]

$$\mathrm{FWHM} = 2.36\hbar\sqrt{S\coth\left(\frac{\hbar}{2kT}\right)} \quad (7)$$

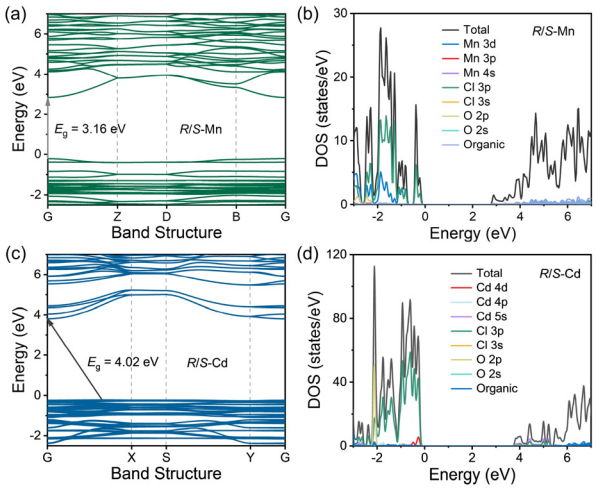


**Fig. 4** (a) The electronic band structures of *R*/*S*-Mn. (b) Density of states (DOS) of *R*/*S*-Mn. (c) The electronic band structures of *R*/*S*-Cd. (d) DOS of *R*/*S*-Cd.

The fitted Huang–Rhys factor $S$ = 6.9 (Fig. S7b†), where $S$ indicates stronger electron–phonon coupling in *R*/*S*-Cd, promoting the formation of STEs. Excitation wavelength-dependent PL spectra (Fig. 3g) show that the PL emission peak at 401 nm is not shifted under the excitation wavelength from 280 nm to 300 nm, contributing to an independent electron-transition channel of $Cd^{2+}$. When the excitation wavelength is increased to above 310 nm, the PL emission of *R*/*S*-Cd is dominated by the singlet-state transition ($S_1$–$S_0$) of $[R/S\text{-}C_5H_{14}N_2]^{2+}$. It is concluded that there is a reverse energy transfer from the inorganic chain to the organic cation in *R*/*S*-Cd.

Both the direct band gaps of *R*/*S*-Mn are calculated to be 3.16 eV, as shown in Fig. 4a. The total density of states (TDOS) and the partial density of states (PDOS) indicate that the valence band maximum (VBM) consists of inorganic units while the conduction band minimum (CBM) consists of inorganic units and organic units (Fig. 4b). Both the indirect band gaps of *R*/*S*-Cd are calculated to be 4.02 eV, as shown in Fig. 4c. The TDOS and PDOS of *R*/*S*-Cd in Fig. 4d indicate that both the VBM and CBM consist of inorganic units, coinciding with the corresponding charge densities (Fig. S8†). In view of this, the photo-physical mechanism is presented in Fig. 3d and h, and the electrons undergo transition from the ground state to the excited state under light excitation. As for the organic component, the electrons are excited from $S_0$ to $S_n$, whose excited electrons at higher energy levels relax to the lowest excited state ($S_1$) and then return to the ground state $S_0$ to realize the singlet-state ($S_1$–$S_0$) fluorescence emission. In the case of *R*/*S*-Mn, the excited $3d^5$ electrons of $Mn^{2+}$ gradually relax to the lowest excited state $^4T_1(G)$, contributing to the

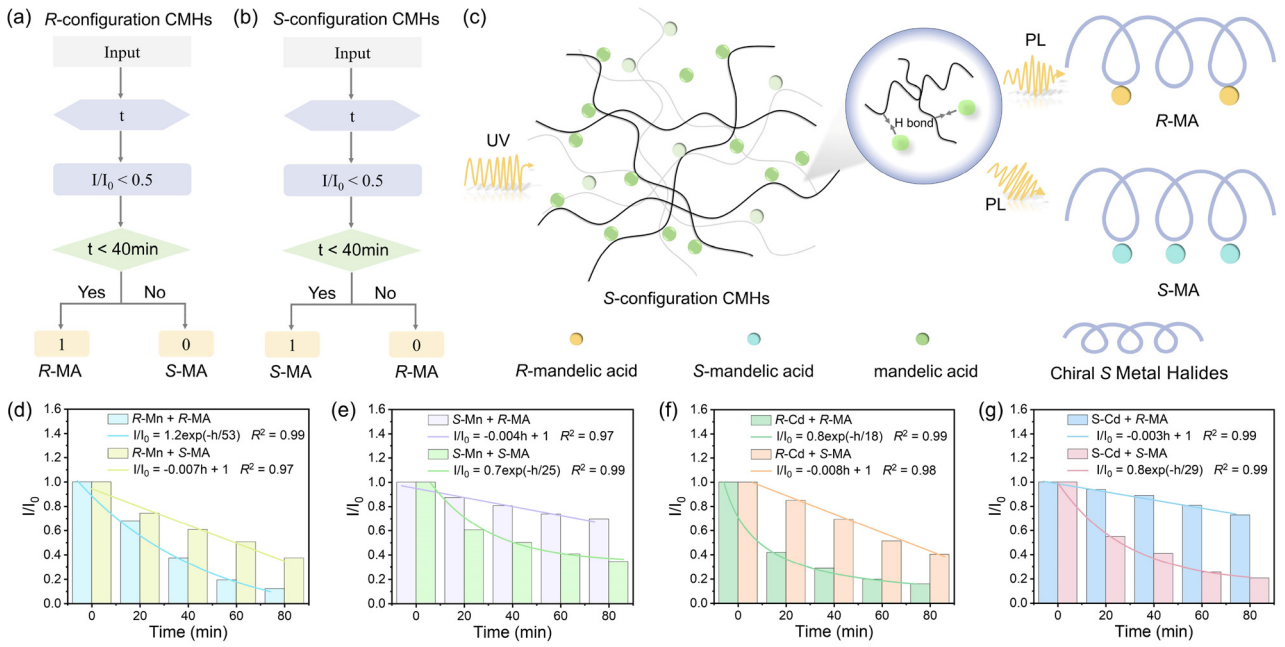


**Fig. 5** Logic gate systems for the recognition of MA based on differences in the PL quenching of *R*-configuration CMHs (a) and *S*-configuration CMHs (b). (c) Schematic diagram of identifying MA based on differences in the PL quenching of *S*-configuration CMHs. PL intensity reduction curves and fitting curves of *R*-Mn (d), *S*-Mn (e), *R*-Cd (f) and *S*-Cd (g) in *R* or *S*-MA.

Published on 12 September 2024. Downloaded on 6/17/2026 6:25:38 PM.

orange emission at 607 nm arising from the d–d transition of $^4T_1(G)$–$^6A_1(S)$. Importantly, there is an energy transfer from the organic cation to the inorganic chain in *R*/*S*-Mn. In contrast, the emission at 401 nm is attributed to the singlet STEs of $Cd^{2+}$ under the strong electron–phonon coupling in *R*/*S*-Cd, accompanied by a reverse energy transfer from the inorganic chain to the organic cation.

Chiral amino acids are essential components for lots of medicines, but amino acid enantiomers usually present diverse pharmacological activities and metabolic processes. *R*-MA (MA = mandelic acid) is a precursor for the synthesis of penicillin, cephalosporins, anti-obesity medicines and anti-neoplastic agents,[46] whereas *S*-MA is a precursor for the synthesis of *S*-bunin.[47] Consequently, the chiral recognition of amino acids has received considerable attention in recent years, in which fluorescence sensing, as one of the methods for recognizing chiral molecules, possesses the merits of simple operation, fast analysis, and excellent selectivity.[48,49] To investigate the fluorescence sensitivity of CMHs, a logic gate system for recognizing *R*/*S*-MA enantiomers was developed according to the PL quenching behaviour in homochiral and heterochiral configurations. The logic gate for *R*-configuration CMHs is shown in Fig. 5a, employing time ($t$) as the input value, where $t$ is the time required for the PL intensity of CMHs to drop below 50% of its initial PL intensity after the addition of MA ($t = I/I_0 < 0.5$), with a threshold value of 40 min. We define that if $t$ is less than 40 min, the output is 1, corresponding to the output of *R*-MA; otherwise the output is 0, corresponding to the output of *S*-MA. Fig. 5b shows the logic gate of *S*-configuration CMHs recognizing *R*/*S*-MA, using the same method of definition, whose outputs are different from those of the *R*-configuration logic gate due to the stereochemical interactions between chiral molecules, with an output at 1 corresponding to *S*-MA and an output at 0 corresponding to *R*-MA. In particular, the PL intensities of *R*/*S*-Mn and *R*/*S*-Cd were quenched with time after the addition of *R*/*S*-MA at the same concentration as shown in Fig. 5d–g, Fig. S9 and S10.† It is noted that the PL intensities were significantly quenched in the presence of homochiral MA. Fig. 5c and Fig. S11† show the schematic diagrams of *R*/*S*-Mn and *R*/*S*-Cd with nitrogenous heterocycles and water sites for the recognition of MA, which form hydrogen-bonding interactions with hydroxyl (–OH) or carbonyl (C═O) in MA to produce fluorescence energy transfer, resulting in quenching of the PL intensity. The difference in PL intensity quenching is attributed to the strong stereoselectivity between CMHs and MA,[50] which confirms that *R*/*S*-Mn and *R*/*S*-Cd can be used for the rapid identification of *R*/*S*-MA, with great potential for the chiral recognition of amino acids.

## Conclusions

In summary, 1D luminescent CMHs were constructed by using *R*/*S*-3-aminopiperidine dihydrochloride as the chiral template, in which the chirality of the organic cation is transferred to the inorganic chain due to the symmetry breaking and helical distortion caused by hydrogen bonding interactions, thus displaying a mirror-symmetric CD signal. In the case of *R*/*S*-Mn, the excited $3d^5$ electrons of $Mn^{2+}$ contribute to the orange emission at 607 nm arising from the d–d transition of $^4T_1(G)$–$^6A_1(S)$, and there is an energy transfer from the organic cation to the inorganic chain. The emission at 401 nm is attributed to the singlet STEs of $Cd^{2+}$ under the strong electron–phonon coupling in *R*/*S*-Cd, accompanied by a reverse energy transfer from the inorganic chain to the organic cation. According to the PL quenching behaviour of CMHs, we innovatively developed a logic gate system for recognizing *R*/*S*-MA enantiomers that benefits from the stereo-selective fluorescence responsivity, thus confirming that *R*/*S*-Mn and *R*/*S*-Cd are useful for the rapid recognition of *R*/*S*-MA.

## Author contributions

S. W. and P. W. performed the experiments, data analysis and wrote the paper. N. Z. performed the DFT calculations. Y. M performed validation and data curation. G. Z. and X. M. Z. conceived the project, wrote the paper, and were primarily responsible for the experiment. All authors contributed to the general discussion.

## Data availability

The data supporting this article have been included as part of the ESI. Crystallographic data for compounds ($R/S$-$C_5H_{14}N_2$)$MCl_4{\cdot}H_2O$ (M = Mn, Cd) have been deposited at the CCDC 2359935–2359938.†

## Conflicts of interest

There are no conflicts to declare.

## Acknowledgements

This work was supported by the National Natural Science Foundation of China (52202177), the Natural Science Foundation of Shanxi Province (20210302124054), and the Shanxi-Zheda Institute for New Material and Chemical Enigeering (2022SX-RF003).

## References

1 J. Ahn, E. Lee, J. Tan, W. Yang, B. Kim and J. Moon, A New Class of Chiral Semiconductors: Chiral-Organic-Molecule-Incorporating Organic-Inorganic Hybrid Perovskites, *Mater. Horiz.*, 2017, **4**, 851–856.
2 S. Li, X. Xu, C. Kocoj, C. Zhou, Y. Li, D. Chen, J. Bennett, S. Liu, L. Quan, S. Sarker, M. Liu, D. Qiu and P. Guo, Large

 This journal is © the Partner Organisations 2024

Published on 12 September 2024. Downloaded on 6/17/2026 6:25:38 PM.

Exchange-Driven Intrinsic Circular Dichroism of a Chiral 2d Hybrid Perovskite, *Nat. Commun.*, 2024, **15**, 2573.

3 C. Chai, Q. Zhang, C. Jing, X. Han, C. Liu, B. Liang, C. Fan, Z. Chen, X. Lei, A. Stroppa, R. Agbaoye, G. Adebayo, C. Zhang and W. Zhang, Single-Component White Circularly Polarized Luminescence in Chiral 1D Double-Chain Perovskites, *Adv. Opt. Mater.*, 2022, **11**, 2201996.

4 J. Lin, D. Chen, L. Yang, T. Lin, Y. Liu, Y. Chao, P. Chou and C. Chiu, Tuning the Circular Dichroism and Circular Polarized Luminescence Intensities of Chiral 2D Hybrid Organic-Inorganic Perovskites through Halogenation of the Organic Ions, *Angew. Chem., Int. Ed.*, 2021, **60**, 21434–21440.

5 C. Liu, H. Li, Y. Chen, D. Xu and Y. Cheng, Circularly Polarized Room-Temperature Phosphorescence Based on Chiral Co-Assembled Helical Nanofiber from Chiral Co-Assembled Liquid Crystal Co-Polymer, *Chem. Eng. J.*, 2024, **486**, 150442.

6 H. Xuan, J. Li, L. Xu, D. Zheng and Z. Chen, Circularly Polarized Luminescence Based on 0d Lead-Free Antimony (III) Halide Hybrids, *Adv. Opt. Mater.*, 2022, **10**, 2200591.

7 X. Niu, Z. Zeng, Z. Wang, H. Lu, B. Sun, H.-L. Zhang, Y. Chen, Y. Du and G. Long, The First Chiral Cerium Halide Towards Circularly-Polarized Luminescence in the UV Region, *Sci. China: Chem.*, 2024, **67**, 1961–1968.

8 Y. Zheng, J. Xu and X. Bu, 1D Chiral Lead Halide Perovskites with Superior Second-Order Optical Nonlinearity, *Adv. Opt. Mater.*, 2021, **10**, 2101545.

9 F. Ge, B. Li, P. Cheng, G. Li, Z. Ren, J. Xu and X. Bu, Chiral Hybrid Copper(I) Halides for High Efficiency Second Harmonic Generation with a Broadband Transparency Window, *Angew. Chem., Int. Ed.*, 2022, **61**, e202115024.

10 M. Li, F. Fang, X. Huang, G. Liu, Z. Lai, Z. Chen, J. Hong, Y. Chen, R.-j. Wei, G.-H. Ning, K. Leng, Y. Shi and B. Tian, Chiral Ligand-Induced Structural Transformation of Low-Dimensional Hybrid Perovskite for Circularly Polarized Photodetection, *Chem. Mater.*, 2022, **34**, 2955–2962.

11 Y. Lu, Q. Wang, R. Chen, L. Qiao, F. Zhou, X. Yang, D. Wang, H. Cao, W. He, F. Pan, Z. Yang and C. Song, Spin-Dependent Charge Transport in 1D Chiral Hybrid Lead-Bromide Perovskite with High Stability, *Adv. Funct. Mater.*, 2021, **31**, 2104605.

12 J. Gao, W. Zhang, Z. Wu, Y. Zheng and D. Fu, Enantiomorphic Perovskite Ferroelectrics with Circularly Polarized Luminescence, *J. Am. Chem. Soc.*, 2020, **142**, 4756–4761.

13 N. Rao, V. M. M. Kumar, V. S. B. Mukherjee, K. N. G. Dutta and A. Das, A Fast Survey on Recent Developments in Designing Colorimetric and Fluorescent Sensors for the Selective Detection of Essential Amino Acids, *Anal. Chem.*, 2023, **15**, 2546–2577.

14 B. Fu, Y. Liu, J. Wang, Z. Zhang and X. Hu, Discrimination of Chiral Amino Acid Enantiomers through Photoelectrochemical Sensing Platform, *Chem. Eng. J.*, 2024, **492**, 152229.

15 C. Li, M. Chong, L. Zhang, B. Tang and L. Bie, All-Inorganic Lead-Free Halide Perovskite $Cs_2TeBr_6$ Enables Real-Time Touchless Human Breath and Finger Related Humidity Monitoring, *Sens. Actuators, B*, 2023, **379**, 133240.

16 D. Li, X. Liu, W. Wu, Y. Peng, S. Zhao, L. Li, M. Hong and J. Luo, Chiral Lead-Free Hybrid Perovskites for Self-Powered Circularly Polarized Light Detection, *Angew. Chem., Int. Ed.*, 2021, **60**, 8415–8418.

17 L. Wang, Y. Xue, M. Cui, Y. Huang, H. Xu, C. Qin, J. Yang, H. Dai and M. Yuan, A Chiral Reduced-Dimension Perovskite for an Efficient Flexible Circularly Polarized Light Photodetector, *Angew. Chem., Int. Ed.*, 2020, **59**, 6442–6450.

18 A. Maiti and A. Pal, Spin-Selective Charge Transport in Lead-Free Chiral Perovskites: The Key Towards High-Anisotropy in Circularly-Polarized Light Detection, *Angew. Chem., Int. Ed.*, 2022, **61**, e202214161.

19 Z. Wang, X. Wang, Z. Chen, Y. Liu, H. Xie, J. Xue, L. Mao, Y. Yan and H. Lu, Turn-on Circularly Polarized Luminescence in Chiral Indium Chlorides by $5s^2$ Metal Centers, *Angew. Chem., Int. Ed.*, 2023, **62**, e202215206.

20 Y. Dang, X. Liu, B. Cao and X. Tao, Chiral Halide Perovskite Crystals for Optoelectronic Applications, *Matter*, 2021, **4**, 794–820.

21 G. Long, R. Sabatini, M. Saidaminov, G. Lakhwani, A. Rasmita, X. Liu, E. Sargent and W. Gao, Chiral-Perovskite Optoelectronics, *Nat. Rev. Mater.*, 2020, **5**, 423–439.

22 H. Lu, C. Xiao, R. Song, T. Li, A. Maughan, A. Levin, R. Brunecky, J. Berry, D. Mitzi, V. Blum and M. Beard, Highly Distorted Chiral Two-Dimensional Tin Iodide Perovskites for Spin Polarized Charge Transport, *J. Am. Chem. Soc.*, 2020, **142**, 13030–13040.

23 Z. Zhu, T. Zhu, J. Wu, S. You, P. Yu, X. Liu, L. Li, C. Ji and J. Luo, Discovering New Type of Lead-Free Cluster-Based Hybrid Double Perovskite Derivatives with Chiral Optical Activities and Low X-Ray Detection Limit, *Adv. Funct. Mater.*, 2023, 2214660.

24 D. Li, J. Song, Z. Xu, Y. Gao, X. Yin, Y. Hou, L. Feng, C. Yue, H. Fei and X. Lei, Reversible Triple-Mode Switching in Photoluminescence from 0D Hybrid Antimony Halides, *Chem. Mater.*, 2022, **34**, 6985–6995.

25 J. Xu, S. Li, C. Qin, Z. Feng and Y. Du, Identification of Singlet Self-Trapped Excitons in a New Family of White-Light-Emitting Zero-Dimensional Compounds, *J. Phys. Chem. C*, 2020, **124**, 11625–11630.

26 Z. Guo, J. Li, C. Wang, R. Liu, J. Liang, Y. Gao, J. Cheng, W. Zhang, X. Zhu, R. Pan and T. He, Giant Optical Activity and Second Harmonic Generation in 2D Hybrid Copper Halides, *Angew. Chem., Int. Ed.*, 2021, **60**, 8441–8445.

27 S. Barman, P. Ranjan and A. Datta, Achiral Phosphonium Induced Remarkable Circular Polarized Luminescence in a Chiral Cadmium(II) Halide Perovskite Material, *Chem. Commun.*, 2023, **59**, 10283–10286.

28 J. Zhao, T. Zhang, X. Dong, M. Sun, C. Zhang, X. Li, Y. Zhao and S. Zang, Circularly Polarized Luminescence from Achiral Single Crystals of Hybrid Manganese Halides, *J. Am. Chem. Soc.*, 2019, **141**, 15755–15760.

Published on 12 September 2024. Downloaded on 6/17/2026 6:25:38 PM.

29 B. Su, G. Zhou, J. Huang, E. Song, A. Nag and Z. Xia, $Mn^{2+}$-Doped Metal Halide Perovskites: Structure, Photoluminescence, and Application, *Laser Photonics Rev.*, 2020, **15**, 2000334.
30 G. Zhou, J. Ding, X. Jiang, J. Zhang, M. Molokeev, Q. Ren, J. Zhou, S. Li and X. Zhang, Coordination Units of $Mn^{2+}$ Modulation toward Tunable Emission in Zero-Dimensional Bromides for White Light-Emitting Diodes, *J. Mater. Chem. C*, 2022, **10**, 2095–2102.
31 D. Liang, H. Xiao, W. Cai, S. Lu, S. Zhao, Z. Zang and L. Xie, $Mn^{2+}$-Based Luminescent Metal Halides: Syntheses, Properties, and Applications, *Adv. Opt. Mater.*, 2023, **11**, 2202997.
32 M. Davydova, L. Meng, M. Rakhmanova, I. Bagryanskaya, V. Sulyaeva, H. Meng and A. Artem'ev, Highly Emissive Chiral Mn(II) Bromide Hybrids for UV-Pumped Circularly Polarized Leds and Scintillator Image Applications, *Adv. Opt. Mater.*, 2023, **11**, 2202811.
33 W. Chen, F. Zhang, C. Wang, M. Jia, X. Zhao, Z. Liu, Y. Ge, Y. Zhang and H. Zhang, Nonlinear Photonics Using Low-Dimensional Metal-Halide Perovskites: Recent Advances and Future Challenges, *Adv. Mater.*, 2021, **33**, 2004446.
34 H. Lu, Z. Vardeny and M. Beard, Control of Light, Spin and Charge with Chiral Metal Halide Semiconductors, *Nat. Rev. Chem.*, 2022, **6**, 470–485.
35 S. Li, J. Xu, Z. Li, Z. Zeng, W. Li, M. Cui, C. Qin and Y. Du, One-Dimensional Lead-Free Halide with near-Unity Greenish-Yellow Light Emission, *Chem. Mater.*, 2020, **32**, 6525–6531.
36 J. Chen, S. Zhang, X. Pan, R. Li, S. Ye, A. Cheetham and L. Mao, Structural Origin of Enhanced Circularly Polarized Luminescence in Hybrid Manganese Bromides, *Angew. Chem., Int. Ed.*, 2022, **61**, e202205906.
37 G. Kresse and J. Furthmuller, Efficient Iterative Schemes for A*b Initio* Total-Energy Calculations Using a Plane-Wave Basis Set, *Phys. Rev. B: Condens. Matter Mater. Phys.*, 1996, **54**, 11169–11186.
38 G. Kresse and D. Joubert, From Ultrasoft Pseudopotentials to the Projector Augmented-Wave Method, *Phys. Rev. B: Condens. Matter Mater. Phys.*, 1999, **59**, 1758–1775.
39 J. Heyd, G. Scuseria and M. Ernzerhof, Hybrid Functionals Based on a Screened Coulomb Potential, *J. Chem. Phys.*, 2003, **118**, 8207–8215.
40 P. Blochl, Projector Augmented-Wave Method, *Phys. Rev. B: Condens. Matter Mater. Phys.*, 1994, **50**, 17953–17979.
41 M. Spackman and D. Jayatilaka, Hirshfeld Surface Analysis, *CrystEngComm*, 2009, **11**, 19–32.
42 P. Spackman, M. Turner, J. McKinnon, S. Wolff, D. Grimwood, D. Jayatilaka and M. Spackman, Crystalexplorer: A Program for Hirshfeld Surface Analysis, Visualization and Quantitative Analysis of Molecular Crystals, *J. Appl. Crystallogr.*, 2021, **54**, 1006–1011.
43 Y. Peng, Y. Yao, L. Li, Z. Wu, S. Wang and J. Luo, White-Light Emission in a Chiral One-Dimensional Organic-Inorganic Hybrid Perovskite, *J. Mater. Chem. C*, 2018, **6**, 6033–6037.
44 L. Yan, M. Jana, P. Sercel, D. Mitzi and W. You, Alkyl-Aryl Cation Mixing in Chiral 2D Perovskites, *J. Am. Chem. Soc.*, 2021, **143**, 18114–18120.
45 X. Zhou, W. Geng, J. Li, Y. Wang, J. Ding and Y. Wang, An Ultraviolet-Visible and near-Infrared-Responded Broadband NIR Phosphor and Its NIR Spectroscopy Application, *Adv. Opt. Mater.*, 2020, **8**, 1902003.
46 X. Zhang, C. Wang, X. Cai, Y. Xue, Z. Liu and Y. Zheng, Upscale Production of (R)-Mandelic Acid with a Stereospecific Nitrilase in an Aqueous System, *Bioprocess Biosyst. Eng.*, 2020, **43**, 1299–1307.
47 Q. Huang, Y. Tao, H. Li, L. Guo, L. Wang, C. Ban and G. Shen, (R,S)-Mandelic Acid in Pure and Binary Solvents Solubility Measurement and Its Correlation with Thermodynamic Models, *J. Mol. Liq.*, 2021, **338**, 116768.
48 L. Pu, Enantioselective Fluorescent Recognition of Free Amino Acids: Challenges and Opportunities, *Angew. Chem., Int. Ed.*, 2020, **59**, 21814–21828.
49 Y. Zhou and J. Yoon, Recent Progress in Fluorescent and Colorimetric Chemosensors for Detection Ofamino Acids, *Chem. Soc. Rev.*, 2012, **41**, 52–67.
50 Y. Jeong, H. Kim, J. Ku and J. Seo, Breakdown of Chiral Recognition of Amino Acids in Reduced Dimensions, *Sci. Rep.*, 2020, **10**, 16166.

 This journal is © the Partner Organisations 2024